

Intra-pulse transition between ion acceleration mechanisms in intense laser-foil interactions

H. Padda,¹ M. King,¹ R. J. Gray,¹ H. W. Powell,¹ B. Gonzalez-Izquierdo,¹ L. C. Stockhausen,² R. Wilson,¹ D. C. Carroll,³ R. J. Dance,¹ D. A. MacLellan,¹ X. H. Yuan,^{4,5} N. M. H. Butler,¹ R. Capdessus,¹ M. Borghesi,⁶ D. Neely,^{3,1} and P. McKenna^{1, a)}

¹⁾*SUPA Department of Physics, University of Strathclyde, Glasgow G4 0NG, UK*

²⁾*Centro de Laseres Pulsados (CLPU), Parque Científico, Calle del Adaja s/n. 37185 Villamayor, Salamanca, Spain*

³⁾*Central Laser Facility, STFC Rutherford Appleton Laboratory, Oxfordshire OX11 0QX, UK*

⁴⁾*Key Laboratory for Laser Plasmas (Ministry of Education) and Department of Physics and Astronomy, Shanghai Jiao Tong University, Shanghai 200240, China*

⁵⁾*Collaborative Innovation Center of IFSA (CICIFSA), Shanghai Jiao Tong University, Shanghai 200240, China*

⁶⁾*Centre for Plasma Physics, Queens University Belfast, Belfast BT7 1NN, UK*

Multiple ion acceleration mechanisms can occur when an ultrathin foil is irradiated with an intense laser pulse, with the dominant mechanism changing over the course of the interaction. Measurement of the spatial-intensity distribution of the beam of energetic protons is used to investigate the transition from radiation pressure acceleration to transparency-driven processes. It is shown numerically that radiation pressure drives an increased expansion of the target ions within the spatial extent of the laser focal spot, which induces a radial deflection of relatively low energy sheath-accelerated protons to form an annular distribution. Through variation of the target foil thickness, the opening angle of the ring is shown to be correlated to the point in time transparency occurs during the interaction and is maximised when it occurs at the peak of the laser intensity profile. Corresponding experimental measurements of the ring size variation with target thickness exhibit the same trends and provide insight into the intra-pulse laser-plasma evolution.

^{a)}Electronic mail: paul.mckenna@strath.ac.uk

I. INTRODUCTION

The acceleration of ions from thin foils irradiated by intense laser pulses offers a promising route towards the creation of compact, short pulse beams of energetic ions^{1,2}. Such a source may enable the development of advanced hadron therapy centres^{3–5} and lead to alternative approaches to inertial confinement fusion^{6,7}. The realisation of such applications requires a deep understanding of the role of the various acceleration mechanisms that are known to occur and the development of techniques to optically control the spectral and spatial characteristics of the resultant ion beam.

Recent developments in laser and target manufacture technology have enabled experiments to be undertaken investigating laser-driven ion acceleration from nanometre-thick targets. In this regime a number of ion acceleration mechanisms have emerged as alternatives to the well established target normal sheath acceleration (TNSA) scheme^{8–10}, exhibiting a faster scaling with laser intensity. Two approaches in particular have received significant attention: the radiation pressure acceleration (RPA)^{11–13} and the transparency-enhanced sheath acceleration (or ‘breakout afterburner’, BOA¹⁴) mechanisms. The onset of transparency in thin foils reduces the effectiveness of RPA, but can volumetrically heat electrons to enhance sheath fields in the BOA scheme. There are a number of studies in which ion energy enhancement and/or changes to the energy spectrum have been shown to be consistent with the onset of either RPA^{15,16}, BOA^{17,18} or other energy transfer processes in the transparency regime¹⁹. Time-integrated measurement of ion spectra alone is insufficient to resolve the key underlying dynamics required to determine which mechanism dominates for given target and laser pulse parameters. Moreover, recent work has shown that multiple acceleration mechanisms can occur over the duration of the laser pulse interaction with an ultrathin foil target. Signature features in the spatial-intensity distribution of the resultant ion beam, including the onset of transverse instabilities and differences in the directionality, show that TNSA, RPA and transparency-enhanced processes can all occur at different phases of the interaction^{20–22}.

In this article, a characterisation of the intra-pulse transition from the radiation pressure-dominated to the relativistic transparency regime in ultrathin foil targets is presented. By measuring changes to the divergence of a low-energy, annular component of the proton beam, the time within the laser pulse envelope at which relativistic induced transparency (RIT)

occurs can be inferred. It is shown, using particle-in-cell (PIC) simulations, that the proton ring is formed by RPA-driven expansion of heavier ions at the target rear, which imparts a radial force on the expanding TNSA-proton layer. The diameter of the ring is shown to be maximised when the onset of transparency occurs close to the peak of the pulse. Good agreement is obtained with experimental results on the scaling of the ring size with proton energy and target thickness.

II. SIMULATION RESULTS

To investigate the intra-pulse transition between the different ion acceleration mechanisms in ultrathin foils, 2D simulations were performed using the fully relativistic, PIC code, EPOCH²³. The simulation box was defined as $130\text{ }\mu\text{m} \times 72\text{ }\mu\text{m}$ using 26000×7200 simulation cells with all open boundaries. The target was initialised as a 2D slab of Al^{11+} ions with a density of $60n_c$ (the density of solid aluminium) with a contamination layer of $60n_c\text{ H}^+$ on the rear of the target, where $n_c = m_e \epsilon_0 \omega_L^2 / e^2$ (m_e is the electron rest mass, ϵ_0 is the vacuum permittivity, ω_L is the angular laser frequency and e is the electron charge). Test simulations incorporating an ionisation model demonstrate that the predominant charge state achieved for Al is $q=11+$ for the laser parameters investigated. The electron population is defined to neutralize all of the ions appropriately with an initial temperature set to 10 keV. The thickness, L , of the Al^{11+} slab was varied in the range $L=20\text{-}500\text{ nm}$, with the contamination layer thickness kept constant at 10 nm. The laser pulse was defined to have a Gaussian temporal profile with a full width at half maximum (FWHM) of 570 fs and was focused to a transverse Gaussian profile with a FWHM of $6\text{ }\mu\text{m}$ at the front of the target. The intensity of the laser pulse was set to $2 \times 10^{20}\text{ Wcm}^{-2}$. To account for the laser propagation effects due to the expansion of the front surface²⁴, the target was positioned $30\text{ }\mu\text{m}$ from the incoming laser boundary. Computationally intensive test simulations with contamination layers on both the front and rear sides, and with binary collisions enabled, show that the front surface proton layer is largely ablated and does not propagate through the Al^{11+} ions. With the exception of this behaviour, the addition of binary collisions has negligible impact on the dynamics of the system and these were therefore not included in the simulations reported.

In all simulations it is found that early in the laser-foil interaction (i.e. at the leading edge

of the laser pulse profile), electrons are accelerated from the target front side and propagate to the rear side, where they set up a strong, longitudinal sheath field, driving the TNSA mechanism. In this field, protons expand faster than the Al^{11+} due to their higher charge-to-mass ratio (q/m), resulting in layering of the two ion species. As the laser intensity continues to increase, the radiation pressure results in the laser pulse *hole boring* into the target and drives an increased longitudinal expansion of the Al^{11+} ions at the rear side. The maximum of this expansion occurs at the centre of the laser focal spot, reducing transversely with a Gaussian profile. As the Al^{11+} expands into the rear of the proton layer, the electrostatic field formed at the interface between the two species begins to deflect the slowest protons towards the direction of the local normal to the Al^{11+} expansion profile. This results in radial proton deflection, as shown schematically in Fig. 1(a).

As the laser intensity decreases beyond the peak of the laser pulse interaction, the radiation pressure will continue to drive the transverse motion, but at a reduced rate. This behaviour can be observed in Figs. 1(b-c) for a $L=500$ nm target which does not become relativistically transparent to the laser. Figure 1(b) shows the Al^{11+} and proton number density at $t=700$ fs with $t=0$ fs defined as the time when the peak of the laser pulse interacts with the front surface of the target. The Gaussian expansion profile of the Al^{11+} layer can be seen and by this time step the low energy proton population (in green) have been swept to either side by the induced transverse motion. Figure 1(c) shows the angular distribution of the beam of accelerated protons as a function of time. For $t < -300$ fs, TNSA dominates and there is a divergent beam with no observed splitting. At approximately $t=-300$ fs the radiation pressure is sufficient that the expansion of the Al ions starts deflecting the low energy protons to larger angles. The width of the resulting annular profile, $\Delta\theta$ (effectively the ring diameter in 3D), increases throughout the remainder of the interaction. The target thickness is such that it remains opaque to the laser light. A ring is not produced at higher proton energies (blue in Figs. 1(c,d)).

For a sufficiently thin target, heating and expansion of the electron population will result in it becoming relativistically transparent during the laser pulse interaction. As an example, Figs. 1(d-e) shows the case for $L=40$ nm, for which RIT occurs at $t=20$ fs. As with the thicker target, the relatively low energy proton beam component starts to undergo radial deflection at approximately $t=-300$ fs. However, the overall rate of increase in $\Delta\theta$ is larger due to the increased velocity of expansion of the Al ions. Thus the diameter of the final

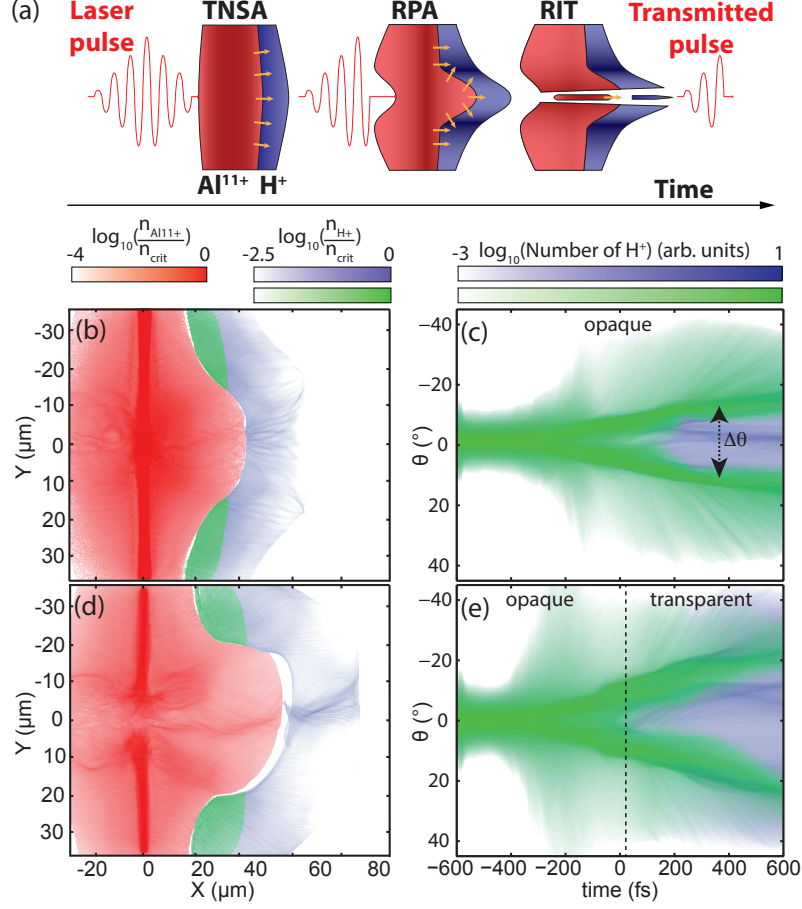


FIG. 1. (a) Schematic, illustrating the three stages of ion acceleration: TNSA driven by energetic electrons early in the interaction; a hole-boring-RPA phase in which Al ions are accelerated into the back of the expanding proton layer, giving rise to radial expulsion; the onset of RIT. (b,c) Example simulation results showing: (b) Ion densities for a $L=500$ nm target at $t=700$ fs after the interaction of the peak of the laser pulse: Red - Al¹¹⁺ ions; Green - protons with energy in the lower quartile; Blue - remainder, higher energy protons. (c) Angular profile of the protons accelerated from the $L=500$ nm target as a function of time with respect to the peak of the pulse ($t=0$). (d,e) Same for $L=40$ nm, with same scales.

proton ring depends on whether RIT occurs and, as will be shown below, on when it occurs with respect to the peak of the laser pulse profile.

Two further observations are worthy of note: (1) The overall target expansion profile is similar to that previously observed experimentally in intense laser pulse interactions with thin foil targets²⁵; (2) A jet of high energy ions can also be observed propagating close to the

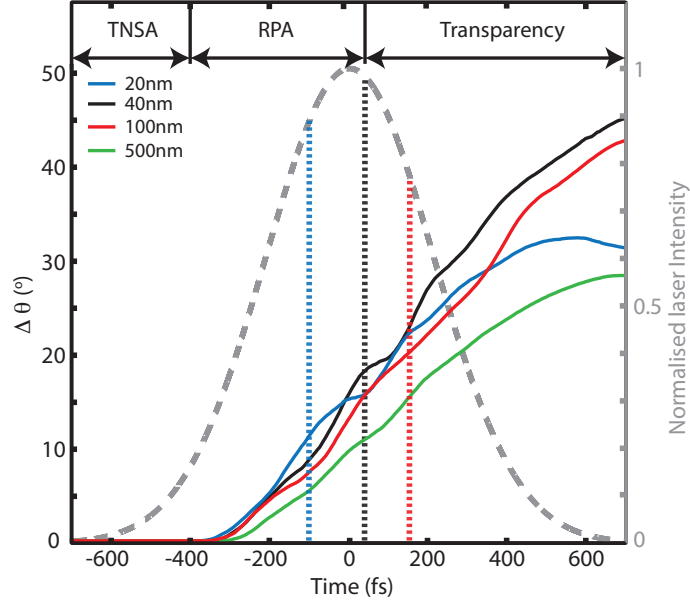


FIG. 2. Simulation results showing the temporal behaviour of the average ring divergence angle for given target thicknesses. The temporal profile of the laser intensity is also shown with dashed vertical lines added to indicate the onset of transparency for the corresponding target thickness. Note that the $L=500$ nm target does not undergo transparency. The dominant intra-pulse acceleration mechanisms are labelled at the top of the figure for the $L=40$ nm example case.

$Y=0$ axis in Fig. 1(d). This is a feature of the transparency-enhanced acceleration regime, as previously reported in Powell *et al*²⁰.

In Fig. 2 the temporal evolution of $\Delta\theta$ is shown for given L in the range 20-500 nm, along with the idealised temporal profile of the laser intensity envelope arriving at the target. In all cases the proton beam splits at around $t=-300$ fs - this occurs slightly earlier for small L and later for large L . As the intensity continues to increase, $\Delta\theta$ increases for all L , but the rate of change differs. The rate is generally higher for small L , within the RPA-dominated phase of the interaction. However, if RIT occurs early in the interaction then the final ring beam diameter is smaller than if it occurs near the peak of the laser profile. This is clearly observed in Fig. 2 when comparing the $L=20$ nm and $L=40$ nm cases (where the dotted vertical line marks the time at which RIT occurs for each L). A comparison with the $L=100$ nm case, for which RIT occurs on the falling edge of the laser pulse, shows that the largest ring is obtained when RIT occurs near the peak of the laser intensity, at which the hole-boring velocity is highest.

III. EXPERIMENT RESULTS

To test the physical picture emerging from the simulation results, an experimental study was performed using the 1.054 μm wavelength Vulcan laser at the Rutherford Appleton Laboratory. This laser delivered pulses of (0.8 ± 0.2) ps FWHM duration, focused to a spot diameter of 8 μm FWHM. A single plasma mirror was employed to increase the intensity contrast from 10^8 to $\sim 10^{10}$ at ~ 40 ps prior to the peak of the pulse.²⁰ This resulted in an on-target laser pulse energy of (200 ± 25) J, giving a calculated peak intensity, $I_L = 2 \times 10^{20}$ W/cm². The laser was linearly-polarized and was aligned at near-normal incidence to Al foil targets with a thickness, L , varied between 10 nm and 400 nm.

The measurement of the spatial-intensity distribution of the beam of accelerated protons

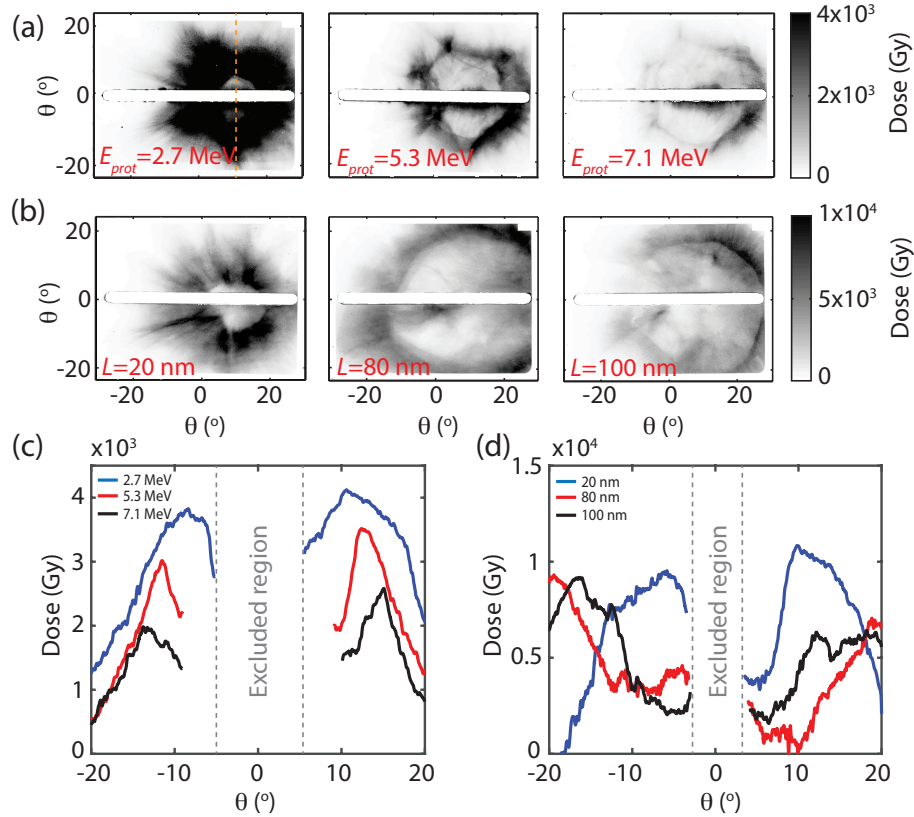


FIG. 3. Measured proton spatial-intensity dose profiles for: (a) Given proton energies ($E_{\text{prot}}=2.7$ -7.1 MeV) for $L=10$ nm; (b) Given L for $E_{\text{prot}}=2.7$ MeV; (c) Vertical line-outs through (a); (d) Vertical line-outs through (b). The angular range missing in (c) and (d) is due to a slot in the RCF.

was achieved using a stack of dosimetry (radiochromic, RCF) film with dimensions of 6.5 cm \times 5.0 cm. This enabled the spatial distribution to be measured in discrete energy bands for E_{prot} ranging from 2.7 to 45 MeV. A horizontal slot was cut through the center of the stack in order to provide a line-of-sight to additional diagnostics and the stack was positioned 6 cm from the rear of the target. A thin PTFE film was also positioned at the front of the stack and the diffuse light generated by the transmitted laser light was imaged using a CCD camera.

An annular beam profile was observed for low energy protons, as shown in the representative measurements of the spatial-intensity profile in Figs. 3(a-b) and corresponding dose profiles along the vertical axis shown in Figs. 3(c-d). For fixed $L=10$ nm, $\Delta\theta$ of the inner part of the ring can be seen to increase with E_{prot} , as shown in Figs. 3(a,c). For higher E_{prot} , the annular structure becomes undetectable, resulting in a low divergent, high energy component as seen in prior studies^{20,26}. In Figs. 3(b,d), $\Delta\theta$ is also observed to vary with L , and is largest for $L=80$ nm. For thinner targets radial instabilities (manifested in spoke structures) can also be observed and may be associated with RIT effects. A more detailed investigation of these instabilities is outside the scope of this article and will be the subject of follow-on work.

Figure 4 compares the quantitative results from the experiment and simulations. As observed in Fig. 4(a), both exhibit an optimal target thickness, L_{opt} , that produces the largest divergence angle in the low-energy proton ring. The difference in the absolute value ($L_{opt}=80$ nm in the experiment and 40 nm in the simulations) is attributed to the idealised parameters and 2D dimensionality of the simulations. A comparison with Fig. 2 reveals that L_{opt} corresponds to the scenario in which RIT occurs at (or close to) the peak of the laser pulse profile. When the target thickness in the simulation results is scaled up by a factor of two to take account of this, good agreement is observed with the experiment results over most of the thickness range. For $L \geq 400$ nm the simulations continue to show a transverse deflection of the lowest energy protons, whereas the ring is not observed experimentally. It should be noted though, that the maximum measured proton energy decreases with increasing L , and as the ring is only produced in the low energy proton population, it is possible that it exists at energies below the lower detection threshold (equal to 2 MeV) of the dosimetry film stack. Otherwise, the overall measured scaling of the ring size with target thickness is similar to that predicted in the simulations.

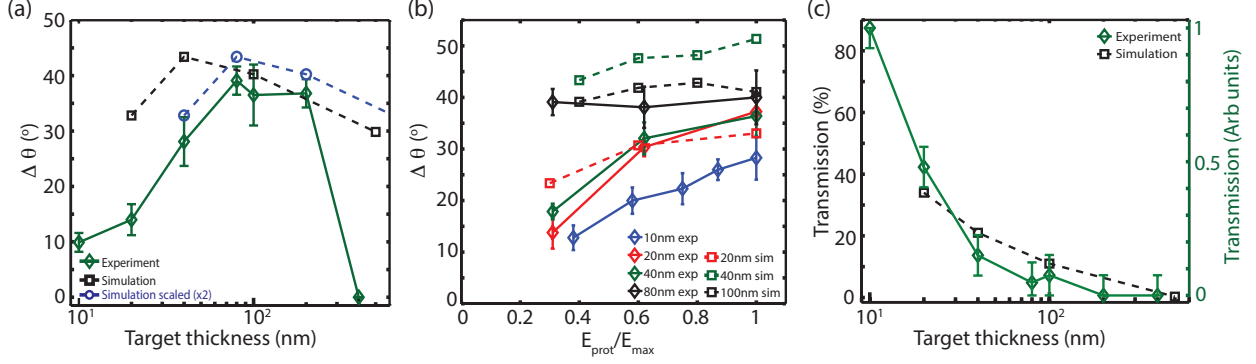


FIG. 4. Comparison of experiment and simulation results. (a) $\Delta\theta$ as a function of L , for low energy protons ($E_{\text{prot}}=2.7$ MeV in the experiment and integrated over the lower 20% of the proton energy range in the simulations). The simulation results scaled by a factor of two in target thickness (as determined by the difference in L_{opt}) is also shown. (b) Divergence angle $\Delta\theta$ as a function of normalised proton energy. (c) Transmitted laser light as a function of L .

Figure 4(b) presents $\Delta\theta$ as a function of E_{prot} , normalised to the maximum proton energy (E_{max}) of the detected annular component. This is shown experimentally for $L=10$ -80 nm and compared with the simulations for $L=20$ -100 nm. The energy dependence of $\Delta\theta$ follows a similar trend in both cases. For $L < L_{\text{opt}}$, the increase in $\Delta\theta$ with E_{prot} is much greater than for $L \geq L_{\text{opt}}$, which further highlights the change in behaviour when $L=L_{\text{opt}}$.

Figure 4(c) displays the measured transmitted light as a function of L , alongside the laser energy transmitted in the simulations. The percentage of laser light transmitted is observed to decrease with increasing L , as expected. For $L \geq L_{\text{opt}}$ (where $\Delta\theta$ varies little with proton energy), the percentage of transmitted light is low. It increases rapidly with decreasing L for $L < L_{\text{opt}}$. Thus the onset of RIT is shown to change the ion expansion dynamics, and thereby the proton ring diameter, and how this varies with proton energy.

IV. DISCUSSION

In conclusion, analysis of the angular emission of the low energy component of the beam of accelerated protons provides new insight into ultrathin target dynamics during ion acceleration. In particular, monitoring how the annular low energy components vary as a function of target thickness can be used to identify the transition between RPA and transparency enhanced charged particle dynamics, and to select the appropriate targets for investigating

either mechanism. This approach can be combined with measurements of the laser transmission, and possibly the duration of the transmitted pulse, to provide new insight into the intra-pulse interaction dynamics, advancing the development of laser-driven ion-acceleration.

ACKNOWLEDGEMENTS

We acknowledge the support of Central Laser Facility staff and the use of the ARCHIE-WeST and ARCHER computers. This work is supported by EPSRC (grants: EP/J003832/1, EP/L001357/1, EP/K022415/1, EP/M018091/1 and EP/L000237/1), the US Air Force Office of Scientific Research (grant: FA8655-13-1-3008) and the European Unions Horizon 2020 research and innovation program (grant agreement No 654148 Laserlab-Europe). LCS acknowledges the EU-funded LA3NET consortium (grant: GA-ITN-2011-289191) and XHY acknowledges support from the National Basic Research Program of China (grant 2013CBA01502). EPOCH was developed under EPSRC grant EP/G054940/1. Data associated with research published in this paper is accessible at [insert DOI].

REFERENCES

- ¹H. Daido, M. Nishiuchi and A. S. Pirozhkov. Rep. Prog. Phys. **75**, 056401 (2012)
- ²A. Macchi, M. Borghesi and M. Passoni. Rev. Mod. Phys. **85**, 751 (2013)
- ³S. V. Bulanov, T. ZH. Esirkepov, V. S. Khoroshkov, A. V. Kuznetsov and F. Pegoraro. Phys. Lett. A **299**, 240 (2002)
- ⁴E. Fourkal, B. Shahine, M. Ding, J. S. Li, T. Tajima and C. -M. Ma. Med. Phys. **29**, 2788 (2002)
- ⁵V. Malka, S. Fritzler, E. Lefebvre, E. d’Humieres, R. Ferrand, G. Grillion, C. Albaret, S. Meyroneinc, J. Chambaretm A. Antonetti and D. Hulin. Med. Phys. **31**, 1587 (2004)
- ⁶M. Roth, T. E. Cowan, M. H. Key, S. P. Hatchett, C. Brown, W. Fountain, J. Johnson, D. M. Pennington, R. A. Snavely, S. C. Wilks, K. Yasuike, H. Ruhl, F. Pegoraro, S. V. Bulanov, E. M. Campbell, M. D. Perry, and H. Powell. Phys. Rev. Lett. **86**, 436 (2001)
- ⁷M. Temporal, J.J. Honrubia and S. Atzeni, Phys. Plasma. **15**, 052702 (2008)
- ⁸E. L. Clark, K. Krushelnick, J. R. Davies, M. Zepf, M. Tatarakis, F. N. Beg, A. Machacek, P. A. Norreys, M. I. K. Santala, I. Watts, and A. E. Dangor. Phys. Rev. Lett. **84**, 670

- (2000)
- ⁹A. Maksimchuk, S. Gu, K. Flippo, D. Umstadter, and V. Yu. Bychenkov. Phys. Rev. Lett. **84**, 4108 (2000)
- ¹⁰R. A. Snavely, M. H. Key, S. P. Hatchett, T. E. Cowan, M. Roth, T. W. Phillips, M. A. Stoyer, E. A. Henry, T. C. Sangster, M. S. Singh, S. C. Wilks, A. MacKinnon, A. Offenberger, D. M. Pennington, K. Yasuike, A. B. Langdon, B. F. Lasinski, J. Johnson, M. D. Perry, and E. M. Campbell. Phys. Rev. Lett. **85**, 2945 (2000)
- ¹¹T. Esirkepov, M. Borghesi, S. V. Bulanov, G. Mourou, and T. Tajima. Phys. Rev. Lett. **92**, 175003 (2004)
- ¹²A. Macchi, S. Veghini, and F. Pegoraro. Phys. Rev. Lett. **103**, 085003 (2009)
- ¹³A. Henig, S. Steinke, M. Schnrer, T. Sokollik, R. Hrlein, D. Kiefer, D. Jung, J. Schreiber, B. M. Hegelich, X. Q. Yan, J. Meyer-ter-Vehn, T. Tajima, P. V. Nickles, W. Sandner, and D. Habs. Phys. Rev. Lett. **103**, 245003 (2009)
- ¹⁴L. Yin, B. J. Albright, B. M. Heglich and J. C. Fernandez. Laser Part. Beams **24**, 291 (2006)
- ¹⁵A. Macchi, S. Veghini, T. V. Liseykina, and F. Pegoraro. New J. Phys. **12**, 045013 (2010)
- ¹⁶S. Kar, K. F. Kakolee, B. Qiao, A. Macchi, M. Cerchez, D. Doria, M. Geissler, P. McKenna, D. Neely, J. Osterholz, R. Prasad, K. Quinn, B. Ramakrishna, G. Sarri, O. Willi, X. Y. Yuan, M. Zepf, and M. Borghesi. Phys. Rev. Lett. **109**, 185006 (2012)
- ¹⁷L. Yin, B. J. Albright, B. M. Hegelich, K. J. Bowers, K. A. Flippo, T. J. T. Kwan and J. C. Fernandez. Phys. Plasma **14**, 056706 (2007)
- ¹⁸D. Jung, B. J. Albright, L. Yin, D. C. Gautier, R. Shah, S. Palaniyappan, S. Letzring, B. Dromey, H. C. Wu and T. Shimada. New J. Phys. **15**, 123035 (2013)
- ¹⁹S. Palaniyappan, C. Huang, D. C. Gautier, C. E. Hamilton, M. A. Santiago, C. Kreuzer, A. B. Sefkow, R. C. Shah and Juan C. Fernandez. Nat. Comms. **6**, 10170 (2015)
- ²⁰H. W. Powell, M. King, R. J. Gray, D. A. MacLellan, B. Gonzalez-Izquierdo, L. C. Stockhausen, G. Hicks, N. P. Dover, D. R. Rusby, D. C. Carroll, H. Padda, R. Torres, S. Kar, R. J. Clarke, I. O. Musgrave, Z. Najmudin, M. Borghesi, D. Neely and P. McKenna. New J. Phys. **17**, 103033 (2015)
- ²¹F. Wagner, S. Bedacht, V. Bagnoud, O. Deppert, S. Geschwind, R. Jaeger, A. Ortner, A. Tebartz, B. Zielbauer, D. H. H. Hoffmann and M. Roth. Phys. Plasma **22**, 063110 (2015)

- ²²B. Gonzalez-Izquierdo, R. J. Gray, M. King, R. J. Dance, R. Wilson, J. McCreadie, N. M. H. Butler, R. Capdessus, S. Hawkes, J. S. Green, M. Borghesi, D. Neely and P. McKenna. *Nat. Phys.* **12**, 505 (2016)
- ²³T. D. Arber, K. Bennett, C. S. Brady, A. Lawrence-Douglas, M. G. Ramsay, N. J. Sircombe, P. Gillies, R. G. Evans, H. Schmitz, A. R. Bell and C. P. Ridgers. *Plasma Phys. Control Fusion* **57**, 113001 (2015)
- ²⁴R. J. Gray, D. C. Carroll, X. H. Yuan, C. M. Brenner, M. Burza, M. Coury, K. L. Lancaster, X. X. Lin, Y. T. Li, D. Neely, M. N. Quinn, O. Tresca, C-G. Wahlstrm and P. McKenna. *New J. Phys.* **16**, 113075 (2014)
- ²⁵S. Kar, M. Borghesi, S. V. Bulanov, M. H. Key, T. V. Liseykina, A. Macchi, A. J. Mackinnon, P. K. Patel, L. Romagnani, A. Schiavi, and O. Willi. *Phys. Rev. Lett.* **100**, 225004 (2008)
- ²⁶N. Dover, C. A. J. Palmer, M. J. V. Streeter, H. Ahmed, B. Albertazzi, M. Borghesi, D. C. Carroll, J. Fuchs, R. Heathcote, P. Hilz, K. F. Kakolee, S. Kar, R. Kodama, A. Kon, D. A. MacLellan, P. McKenna, S. R. Nagel, D. Neely, M. M. Notley, M. Nakatsutsumi, R. Prasad, G. Scott, M. Tampo, M. Zepf, J. Schreiber and Z. Najmudin. *New J. Phys.* **18**, 013038 (2016)